



Study on the Correlation Mechanism Between Wear Failure Behavior and the TRIP Effect of Retained Austenite in Bainitic Steel

Peng Chen^{1,2} · Sida Chen^{1,2} · Qinyuan Huang^{1,2} · Wen Zhang³ · Zulai Li^{1,2} · Hong Wu⁴ · Quan Shan^{1,2}

Received: 28 April 2023 / Accepted: 3 June 2023 / Published online: 19 June 2023
© The Author(s), under exclusive licence to Springer Science+Business Media, LLC, part of Springer Nature 2023

Abstract

Clarification of wear behaviors would be attractive for selecting and designing wear-resistant materials. In this study, the wear behaviors of bainitic and martensitic wear-resistant steels (FB and H400) were investigated under different wear conditions. Comparing the wear resistance of FB with that of H400 specimen, the former was inferior to the latter under three-body abrasive wear, but the opposite was true based on the impact wear results. FB, composed of bainite, martensite, and retained austenite (RA), exhibited lower resistance against abrasive cutting because of its lower hardness and yield strength. The H400, composed of high-hardness martensite, displayed great three-body abrasive resistance, but the wear behavior changed when impact wear was introduced. In addition, the fatigue triggered by the impact of the wear surface played a greater role. The FB with RA had higher plasticity because of the transformation-induced plasticity (TRIP) effect, which could delay fatigue crack growth. Therefore, the FB demonstrated better wear resistance under impact wear.

Keywords Bainitic wear-resistant steel · Wear behavior · Retained austenite · Impact wear · Fatigue crack · TRIP effect

1 Introduction

The selection of materials is crucial to engineering safety, especially under demanding working conditions [1], such as mining, machinery, rail transit, and mineral transport. At present, the relative movement of the workpiece under two-body wear, the cutting and embedding of abrasives on the material surface under three-body abrasive wear, and the impact loading under impact wear are the main wear problems encountered by materials. It is generally accepted that

hardness is directly proportional to wear resistance [2], and improving the surface hardness is an effective way to solve the wear problem. However, high hardness is usually accompanied by low toughness, which negatively affects the wear resistance under impact wear conditions [3–5]. Especially in the service environment, wear parts are constantly impaired by the impact and sliding of crushed ore, such as the middle trough plate of a scraper conveyor and ball mill liner [6, 7]. Inappropriate selection of high-hardness wear-resistant materials often seriously deteriorate the service stability and reduce the life of engineering components under these working conditions, and even causes serious economic and safety problems.

Scholars have begun to study the difference in wear resistance of martensitic and bainitic steels with similar hardness in wear conditions [8–11]. Shah et al. [10] found that carbide-free bainite exhibited higher wear resistance under three-body abrasive wear. In their study, the higher wear resistance of bainitic steels was associated with the transformation of retained austenite (RA) to martensite. Because the transformation-induced plasticity (TRIP) effect of RA could enhance plasticity and toughness [12–16], and the newly formed martensite could also increase the surface hardness [17, 18]. It was also found that martensitic wear-resistant steel exhibited high wear resistance under three-body abrasive wear condition

✉ Hong Wu
hwucsu@csu.edu.cn

✉ Quan Shan
quanshan.ms@gmail.com

¹ Faculty of Material Science and Engineering, Kunming University of Science and Technology, Kunming 650093, China

² National & Local Joint Engineering Laboratory for Technology of Advanced Metallic Solidification Forming and Equipment, Kunming 650093, China

³ Yunnan Kungang Wear Resistant Material Science Co., Ltd., Kunming 650093, China

⁴ State Key Laboratory of Powder Metallurgy, Central South University, Changsha 410083, China

[19, 20]. However, their main research work still focused on a single wear condition. Wei et al. [11] further studied the wear behavior of bainitic and martensitic microstructures with similar hardness and fracture toughness under different wear conditions. They found that the stability of RA affected the wear resistance of bainitic steels. The wear condition selected in these studies above introduced the abrasive wear, and abrasive cutting will accelerate the weight loss of the specimen. However, the propagation of dislocations and fatigue cracks during wear progress remain to be studied, which could affect the wear resistance of the material. Moreover, in non-abrasive working conditions, such as jaw crusher, and impact crusher, which are only subjected to impact loading, the failure of the material is different compared with abrasive wear conditions. If the selection and matching of high-strength wear-resistant steel under different wear conditions can be systematically measured, it can provide a theoretical basis for improving the service and safety of wear-resistant parts.

To provide a reference for selecting and designing suitable material under different wear conditions, the wear behavior of selected bainitic wear-resistant steel (forged bainitic steel, FB) and martensite wear-resistant steel (Hardox400, H400) was investigated under three-body abrasive wear (excavator bucket) and impact wear (impact crusher). We discussed the wear mechanism under different wear conditions and analyzed the relationship between microstructure and wear resistance. Based on the classical Williamson-Hall, the density of dislocation during impact wear progress was analyzed. In addition, the reasons for the difference in material weight loss due to fatigue cracking were analyzed using a designed three-point bending test.

2 Experiment Method

2.1 Chemical Composition of Materials

Commercial wear-resistant steel (Hardox400, H400) was received as heavy plate with dimensions of 300 mm × 1000 mm × 40 mm. H400 obtained high hardness and wear resistance through an effective quenching process. The FB specimens were smelted in a vacuum induction furnace to produce 50 kg ingots of dimension 160 × 160 × 250 mm³. The specimen was heated to 1250 °C and held for 1 h. Then cooled to 1000 °C for upsetting and drawing with a forge ratio of 7. The final forging temperature was controlled at 900 °C and then air-cooled to room temperature. Finally, the specimen was tempered at

200 °C for 3 h. The density of H400 and FB specimens was measured by the Archimedes drainage method, which was 7.7153 g·cm⁻³ and 7.6822 g·cm⁻³, respectively. The chemical compositions of the FB and H400 specimens are presented in Table 1. The addition of Si to FB significantly reduced the phase transformation drive of Fe₃C, delayed the decomposition of RA to Fe₃C during quenching and tempering, and improved the stability of RA. In contrast, the addition of Mo facilitated the formation of a bainitic structure by air cooling.

2.2 Microstructural Characterization

The microstructures and wear surfaces of the FB and H400 specimens were characterized using scanning electron microscopy (SEM, ZEISS-EVO-18, 30 kV). Specimens that were mechanically ground, polished, and then etched with 4% nitric acid alcohol solution for 5–10 s were used to observe the microstructure. Electron backscatter diffraction (EBSD, Oxford Instruments C-Nano) was used to analyze the composition and distribution of the phases with an acquisition step size of 100 nm. After the mechanical grinding and polishing of the specimens, the residual surface stress was removed by electrolytic polishing (20 kV, 40 s) using a solution of 7% perchloric acid. Transmission electron microscopy (TEM, FEI Tecnai G20) was used to distinguish the specimen microstructures, especially blocky residual austenite (B-RA) and thin-film residual austenite (F-RA). The confocal mode of the three-position morphometry (Rtec, UP-Lambda, USA) was used for macroscopic photography of the wear surface.

The phase transformation in FB specimen was analyzed using X-ray diffraction (XRD, Empyrean Ag LFF (9430 922 0017X) DK4), using Ag K α radiation. The transformation of RA is characterized using XRD during the impact process. Ag target XRD has the characteristics of higher voltage (up to 60 kV, Cu target can only reach 40 kV) and shorter wavelength (only one-third of that of Cu target), so more volume can be observed (from wear surface to subsurface) to reveal more phase transitions detail. The specimens were scanned in the range of 10–45° with an applied voltage of 60 kV and a current of 36 mA in steps of 0.0001° with a dwell time of 300 s per step (25 min for each specimen measurement). The increase in dislocation density can be calculated using the classical Williamson-Hall rule [21, 22] shown below:

Table 1 Chemical composition of FB and H400 (Wt.%)

Material	Fe	C	Si	Mn	Cr	Mo	Ni	B	Cu	N
FB	93.04	0.27	1.49	1.51	1.93	0.42	1.05	0.004	0.29	0.0021
H400	96.55	0.15	0.70	1.60	0.50	0.25	0.25	0.0004	–	–

$$\Delta K = \frac{0.9}{D} + \varepsilon K \quad (1)$$

$$\Delta K = \beta \frac{\cos\theta}{\lambda} \quad (2)$$

$$K = \frac{2\sin\theta}{\lambda} \quad (3)$$

where β is the full width at half-maximum (FWHM) of the spectral line, θ is the Bragg diffraction angle, λ is the X-ray wavelength, D is the grain size, and ε is the microscopic strain. The dislocation density ρ is given by Eq. (4), and it is assumed that the lattice strain is generated only by dislocations:

$$\rho = B \left(\frac{\varepsilon}{b} \right)^2 \quad (4)$$

where b is the Burgers vector size and B is the conversion factor between ε and ρ , estimated to be 14.4 [22].

2.3 Mechanical Properties Tests

The Brinell hardness and Vickers hardness (SHIMADZU HMV-G-FA, Japan) specimens were measured using the same dimensions (10×10×10 mm). For the accuracy of the hardness value, Brinell hardness was tested (using a loading force of 1839N, pressure holding time of 15 s) at three different points on three specimens. Vickers hardness (using a loading force of 980.7mN, pressure holding time of 10 s) was used to characterize the fluctuation of hardness values caused by the microstructural differences. The hardness of the deformed layer after wear test was also characterized using Vickers hardness (using a loading force of 245.2mN, pressure holding time of 10 s). A micro-force fatigue tester (MMT-250N, Japan) was used to measure the fatigue performance of FB and H400 by controlling the downward displacement (0.5 mm). The room-temperature tensile properties of the material were tested using a SHIMADZU AG-X 100 kN tensile tester (Japan) with a strain rate of 0.5×10^{-3} /s. An Impact Pendulum Tester (Zwick/HIT 5.5P) was used for the Charpy impact tests at room temperature (RT, 298 K). The Charpy V-notch specimens with the size of 55×10×10 mm³, and a V-notch depth of 0.8 mm were prepared.

2.4 Wear Tests

The wear test parameters were selected based on our previous work and literature on wear-resistant steels [23, 24]. Three-body abrasive wear (MMH-5, China) selected 40–70 mesh SiC particles as abrasives to test the wear performance of the FB and H400 specimens. The specimens

(30×38×16 mm) were machined by wire cutting, the loading force was maintained at 20 N during the wear process, and the speed was maintained at 30 revolutions per minute (rpm). The impact wear test machine (MLD-10, China) was selected. The speed of the upper specimen was 60 time/min, the rotation speed of the lower specimen was 200 rpm, and the 1.5 J impact work simulated the impact wear condition. The wear testers are shown in Fig. 1. The impact test specimens were machined to 10×10×30 mm, and the contact surface between the upper and lower specimens was made to have the same curvature as the lower type to avoid the change in wear resistance due to the contact area. Three-body abrasive and impact wear specimens were pre-worn for 5 min, each 30 min of wear was defined as a wear process, and the specimens were ultrasonically cleaned and weighed at the end of each wear process. The specimens were tested thrice to ensure the repeatability of the experiment. The weight loss of wear was the average value of the three test results, and the standard deviation was calculated to ensure the repeatability of the data. The weight loss per 30 min was defined as the wear resistance of the material and was calculated using Eq. (5):

$$\text{Wear resistance}(g^{-1}) = \frac{1}{\text{Mass loss per 30min}(g)} \quad (5)$$

3 Results

3.1 Microstructure Analysis of the Experimental Steels

Figure 2 shows the microstructural micrograph of the experimental steels. The H400 specimen exhibited a single-phase structure as a martensitic lath, as shown in

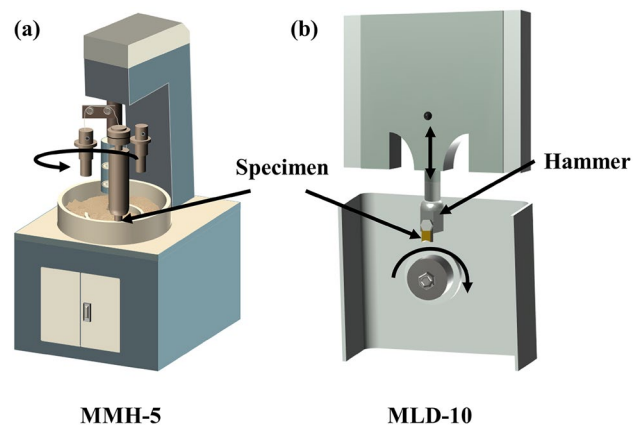


Fig. 1 Schematic illustration of three-body abrasive wear **a** MLD-10) and impact wear **b** MLD-10)

Fig. 2 SEM microstructure of **a** H400 and **b** FB specimens; EBSD phase diagram of **c** H400 and **d** FB; **e** (50 nm) and **f** (30 nm) are EBSD phase diagrams with different acquisition step size of FB specimens; color (blue—martensite, gray—bainite, red—austenite) representation of microstructure and its distribution (Color figure online)

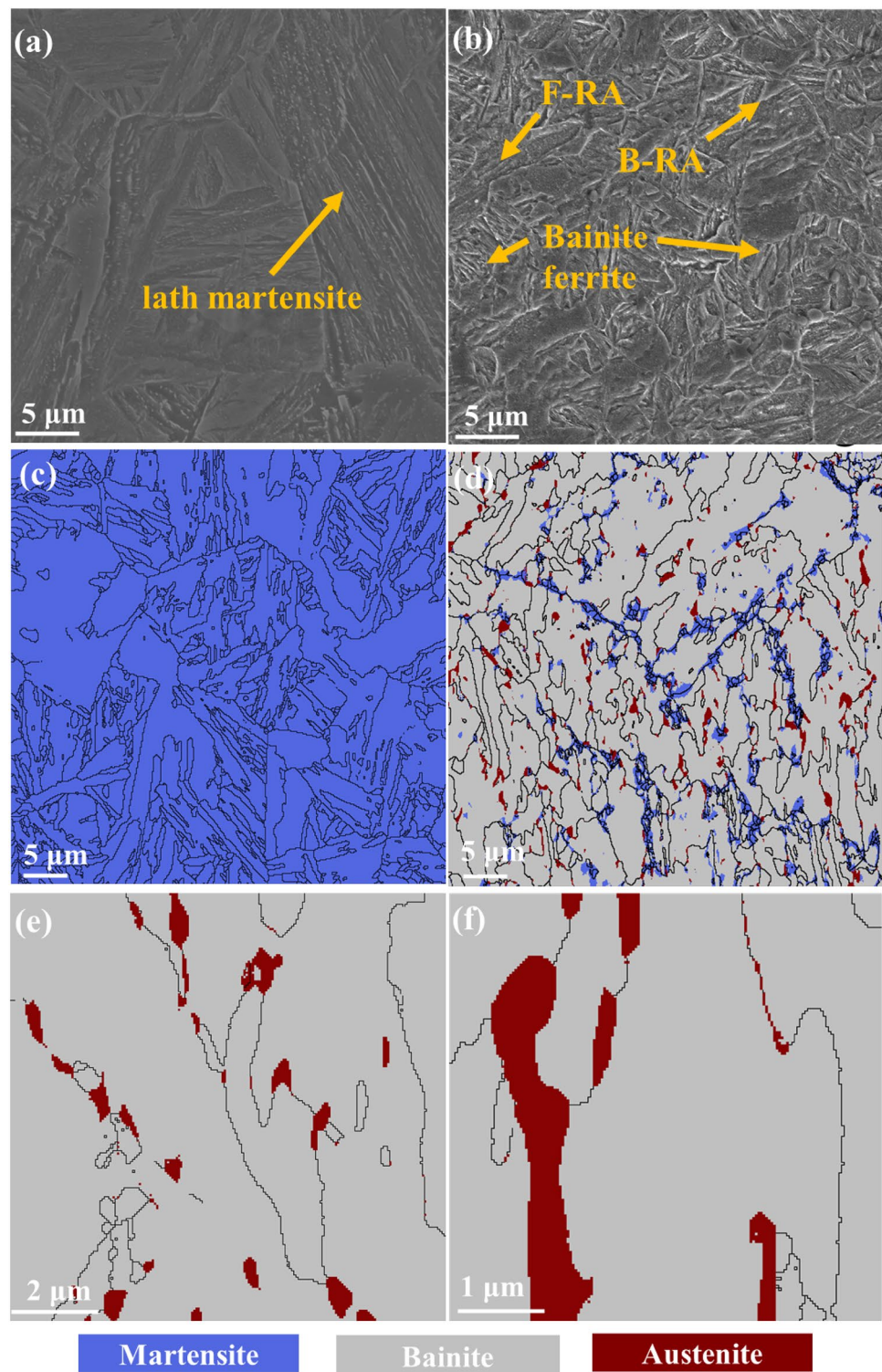


Fig. 2a and c. The FB specimen (Fig. 2b and d) presented a multiphase structure comprised of bainite, martensite, and austenite. Based on the EBSD results, the volume fractions of residual austenite, bainite, and martensite in the FB samples were 4.5%, 86.1%, and 9.4%, respectively. However, the volume fraction of RA calculated from the

XRD pattern was 8%, which was inconsistent with the result calculated by EBSD. The difference in RA volume fraction calculated by XRD and EBSD may be attributed to the fact that the EBSD acquisition step size is too large to collect the data of small-sized RA. To improve the accuracy of EBSD for characterization of RA, we reduced

the acquisition step size of EBSD to 50 nm (Fig. 2e) and 30 nm (Fig. 2f).

The microstructure of RA was further characterized by TEM, as shown in Fig. 3. The RA in the FB sample presented two forms of block RA (B-RA) and film RA (F-RA), and the width of F-RA was about 30 nm. It is generally believed that F-RA and B-RA exhibit different mechanical stability, and the high mechanical stability of F-RA ensures the gradual occurrence of the TRIP effect [25, 26].

According to the observation of the microstructure and the subsequent XRD results, we did not observe the presence of a sufficient amount of cementite. In addition, it had also been found that 1.43% Si content can also form carbide-free bainite [27]. It was important to mention that bainite was carbide-free (at least presumably) since it contributed to wear resistance.

3.2 Mechanical Performance

Figure 4 shows the results of tensile tests at room temperature. The mechanical properties of FB and H400 specimen exhibited little difference except for the total elongation (TE). The ultimate tensile strength (UTS) of the FB

specimen reached 1399 MPa, while that of H400 specimen was only 1351.6 MPa. The TE of FB and H400 specimens was 13.57% and 9.19%, and the uniform elongations were 8.34% and 4.21%, respectively. In addition, the work-hardening rate of FB specimen at the end of uniform plastic deformation was still 199 MPa, while that H400 only had 55 MPa. This multiphase structure of FB specimen was beneficial for obtaining high strength and plasticity. Bainitic bundles will rotate, bend, and elongate during tensile test, which contributed to the high plasticity [28]. In addition, RA in the FB specimen contributes to the strength and elongation during the tensile process [26]. And the TRIP effect of RA can improve the work-hardening rate [29].

Figure 5 displays the GND density in the H400 and FB specimens. This was done by evaluating the degree of local deformation by the average orientation difference between the scanning point and the surrounding area [30]. The GND density of H400 was higher than the FB specimen. The dislocation density distribution of FB specimen was relatively uneven. The dislocation density of the martensitic structure in FB specimen was higher than the bainitic structure, which may be caused by the large back stress with the surrounding bainitic-ferrite structure [31].

Fig. 3 **a** TEM images of FB specimen matrix; **b** TEM dark-field image in **(a)** (When the structure is the same as the RA or the orientation is similar, the same bright white appears in the TEM dark-field image); **c** The selected area diffraction pattern (SAED) of RA in **(a)**

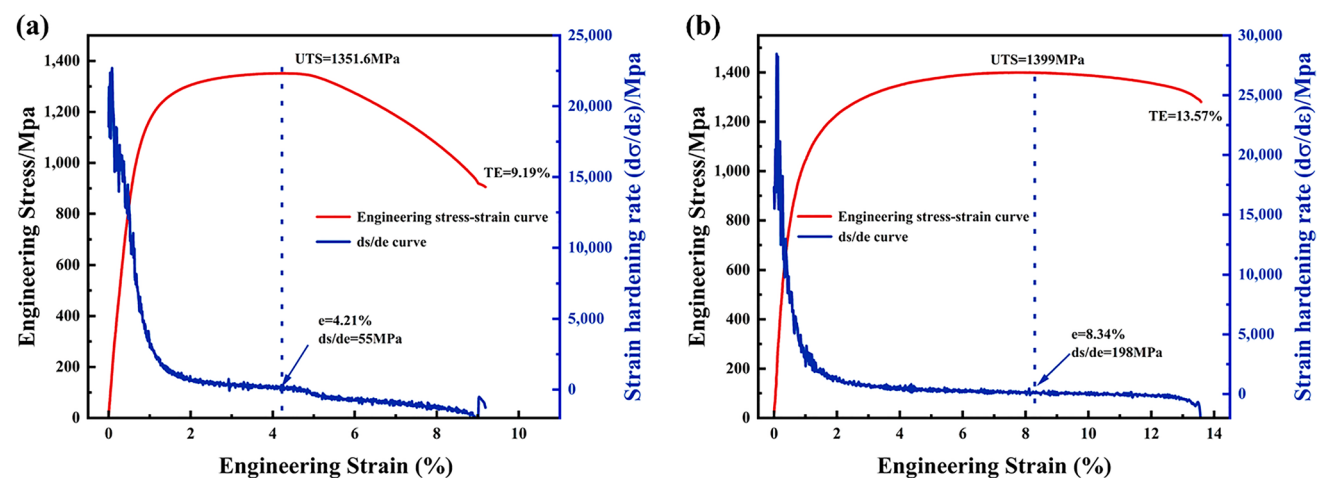
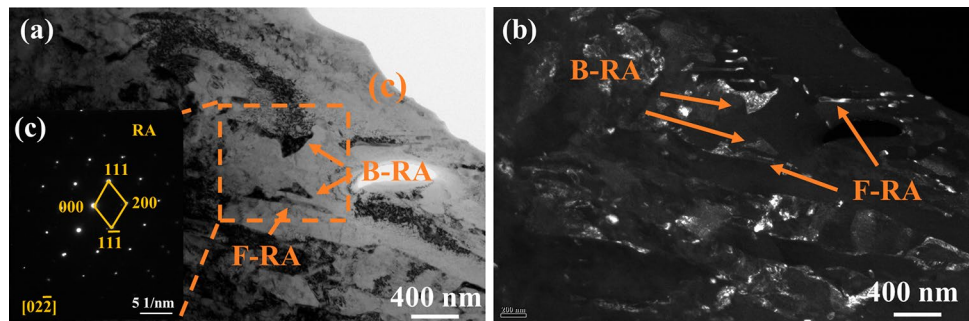


Fig. 4 Engineering stress–strain curves and work-hardening rate curves of **a** H400 and **b** FB specimens

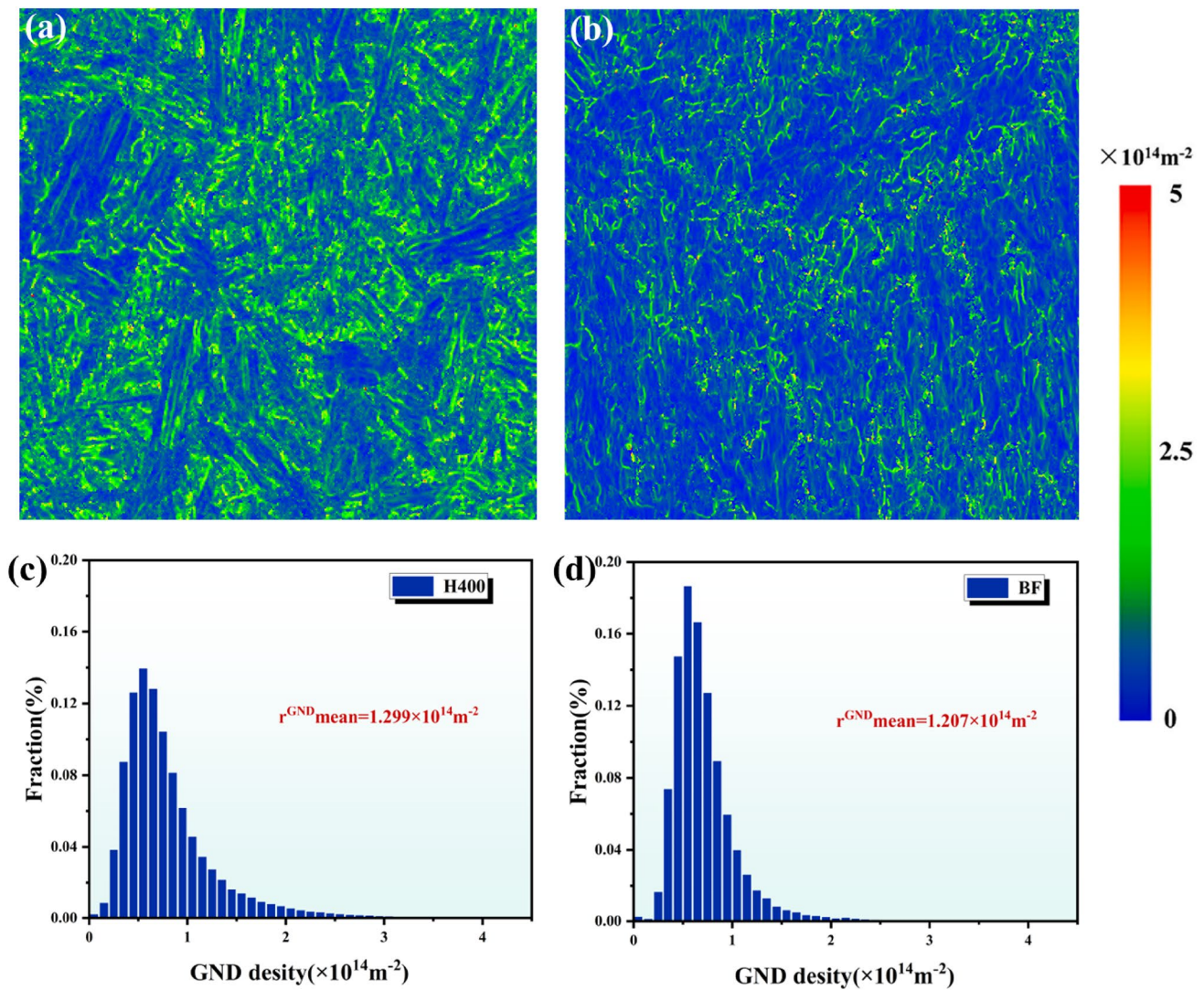


Fig. 5 Geometrically necessary dislocation (GND) density of **a** H400 and **b** BF specimen; quantitative distribution histogram of **c** H400 and **d** BF specimen

Figure 6 depicts the Vickers hardness of H400 and BF specimens. The hardness values of the H400 and BF specimens are listed in Table 2. The hardness range of the H400 specimen was 381–420 HV, and that of the BF specimen was 362–444 HV. The microstructure was responsible for fluctuations in hardness values. In the BF specimens, the hardness of RA was lower than martensitic structure. During the hardness testing, the indenter's contact microstructure was different, resulting in a large difference between the maximum and minimum hardness values. Compared with BF specimen, the hardness fluctuation of H400 was relatively tiny (40HV), which was attributed to the single-phase martensite structure.

3.3 Wear Mechanism

3.3.1 Three-Body Abrasive Wear

The three-body abrasive wear surfaces of BF and H400 specimens are shown in Fig. 7. Under three-body abrasive wear condition, the abrasives embedded in the matrix produced cutting on the matrix during the sliding process. Micro-cutting was the dominant wear mechanism [20, 32, 33]. Ploughing, pits, and abrasives embedded in the matrix were found on the surfaces of the BF and H400 specimens (Fig. 7a, b). Crack appeared at the front of abrasive in BF specimen. In the 3D morphometry, the abrasives caused unevenness to the

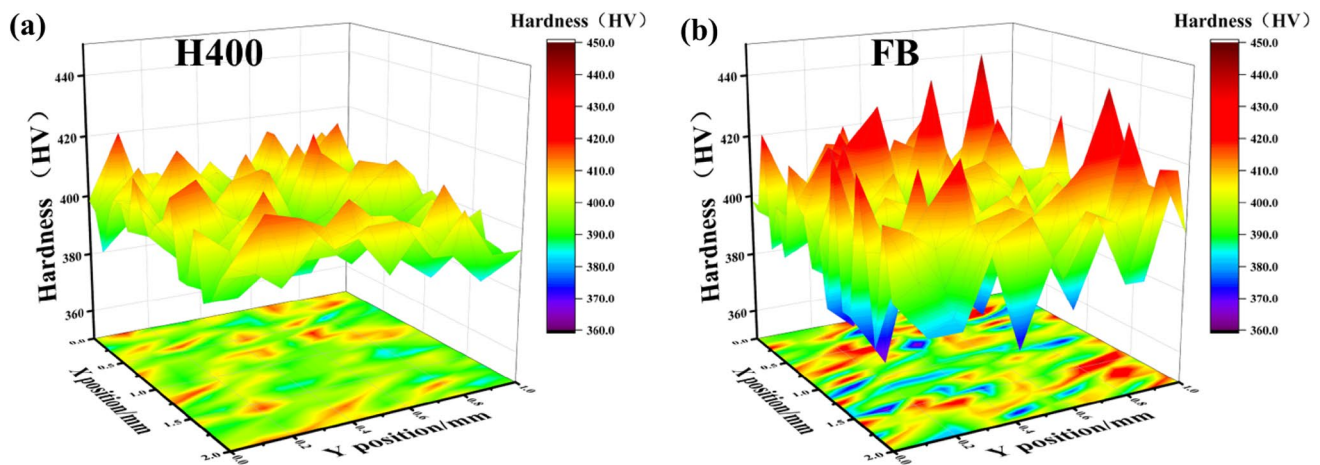


Fig. 6 Color mapping surface diagram of Vickers hardness of Hardox 400 and FB specimens

Table 2 Summary of Vickers hardness, Brinell hardness, and Charpy impact for H400 and FB specimens

Material	Average hardness (HV)	Maximum hardness (HV)	Minimum hardness (HV)	Brinell hardness (HBW)	Charpy impact (J)
H400	398.18 ± 2	419.92	381.11	393 ± 2	39.4 ± 6
FB	399.07 ± 3	443.08	362.59	393 ± 5	48.7 ± 5

shallow area of the H400 specimen with a depth of about 30 μm . In the FB specimen, the macroscopic wear surface differed from H400 specimen. Grooves dominated the wear surface, and the deepest reached 150 μm . It could be inferred from the wear surface that the FB specimen had more weight loss than the H400 specimen during the three-body abrasive wear process.

The specific weight loss statistics of H400 and FB specimens are shown in Fig. 8a. The weight loss of the FB specimen at the end of wear progress was 14.66% higher than that of H400. However, the weight loss at each stage of the wear process was different, indicating that the material's wear resistance changed as the wear time increased. In Fig. 8b, the relative wear resistance of the materials was represented by the reciprocal of weight loss at each stage. Both the FB and H400 specimens showed an increasing trend in wear resistance. The total wear resistance increases of H400 and FB specimens was about 7%. Figure 8c describes the hardness changes of the subsurface layer of H400 and FB specimens. The maximum hardness of FB specimens was 507 HV and that of H400 was 488 HV. Work-hardening may contribute to the increase in wear resistance.

3.3.2 Impact Frictional Wear

There are differences in the statistics of the impact wear weight loss compared with the three-body abrasive wear, as shown in Fig. 9. The cumulative weight loss of FB

specimen after whole wear progress was 7.32% lower than that of H400. The wear resistance curve is shown in Fig. 9b. The wear resistance of FB specimen increased by 11.2%, whereas that of H400 specimen was 6.67%. The FB specimen exhibited lower weight loss under impact wear condition, in contrast to three-body abrasive wear. This may be caused by the changes of the wear surface, work hardening, and microstructure during the impact wear process.

Compared with the three-body abrasive wear, the wear surfaces of H400 and FB changed, as shown in Fig. 10. Micro-cutting remained on the wear surface and the grooves disappeared due to the removal of the abrasive. The wear mechanism changed owing to the change in wear condition, which was dominated by delamination after plastic deformation [17, 34, 35]. Figure 10a shows the uneven wear surface of H400 caused by fatigue spalling. The wear surface of the FB specimen was also uneven (Fig. 10b), and many fatigue cracks were present on the wear surface, which was distinguished from H400. The cause of the weight loss discrepancy is shown in the 3D (Fig. 10c, d). The unevenness of the wear surface of the FB specimen was caused by fatigue spalling and cutting. However, pits appeared on the wear surface of H400 specimen, with a maximum depth of 300 μm far exceeding the 15 μm of FB.

The hardness and SEM micrographs along the normal direction after the impact wear are shown in Fig. 11. Figure 11a and c describes the hardness change in the H400 and FB specimens, and include the impact wear surface to the

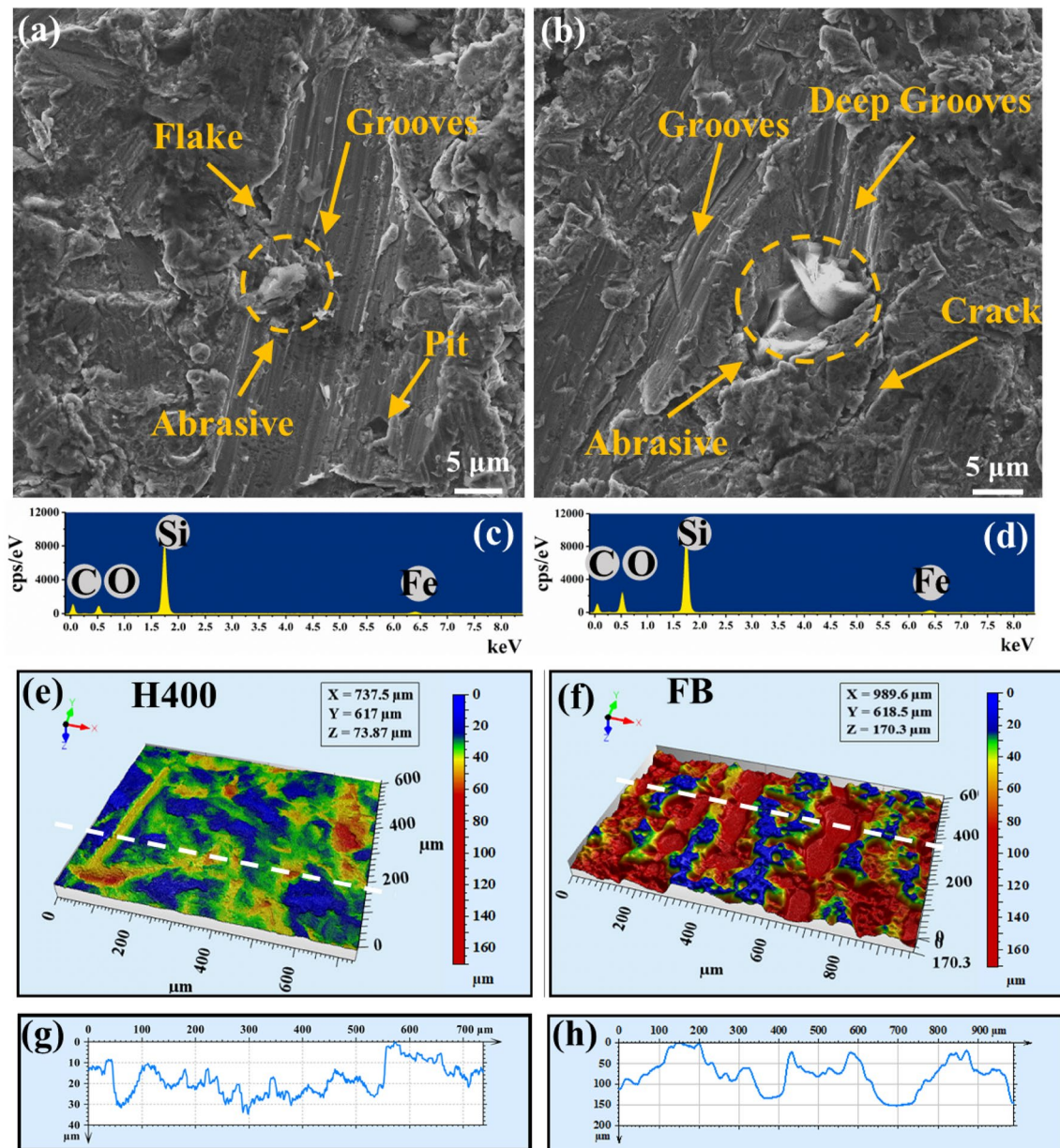


Fig. 7 SEM micrographs of wear surface of **a** H400 and **b** FB specimens; EDS analysis of **c** fractured abrasive in **(a)** and integrity abrasive **(d)** in **(b)**; three-dimensional wear surface of **e** H400 and **f** FB; depth of cross-section statistics for **g** H400 and **h** FB specimens

subsurface layer in the range of a few hundred microns along the normal direction. The main difference was the thickness of the work-hardening layer and maximum hardness of the subsurface. The hardness value of the FB specimen at 340 μm was higher than that of the unwear part. However, H400 returned to the hardness level of the matrix at 60 μm , and the effect of work-hardening basically disappeared. The subsurface hardness of the FB specimen after impact wear test was 970 HV, which was 230% of the average hardness of the matrix. Although the hardness value decreased with increasing distance, it also increased by 50% compared with

the matrix hardness. However, the H400 specimen maximum hardness value only increased by 50% and rapidly decreased to the matrix level.

3.4 XRD Analysis of FB Specimen During Impact Wear Process

The transformation of RA will be characterized using XRD during impact wear progress. Fig. 12 describes the microstructure and dislocation changes of FB specimens after 0, 0.5, 1, 2, and 4 h of impact wear by Ag target XRD.

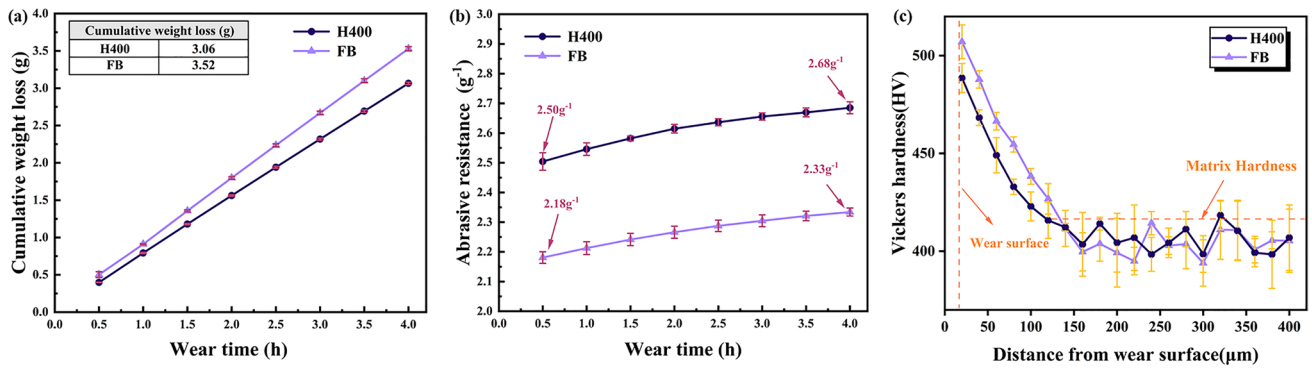


Fig. 8 Cumulative weight loss (a) and wear resistance curve (b) of H400 and FB specimens in three-body abrasive wear; c the hardness of distance from wear surface under three-body abrasive wear of H400 and FB specimens

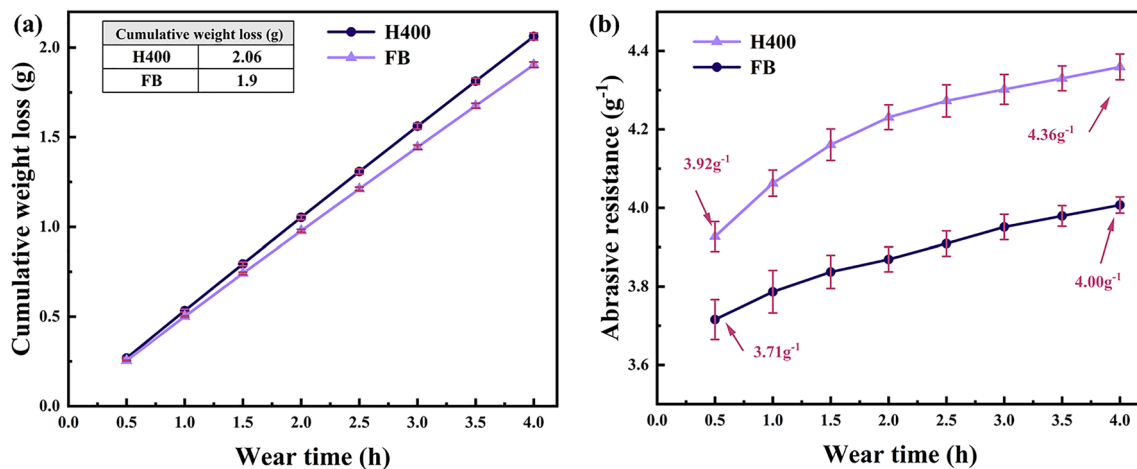


Fig. 9 Cumulative weight loss (a) and wear resistance curve (b) of H400 and FB specimens in impact wear test

The volume fraction of actually transformed RA could not be calculated in the FB wear specimens, because of the increased overall intensity of (200) and (211) of the ferrite peaks (Fig. 12a). We found that the volume fraction of RA decreased with time by locally zooming in the (200) region of the RA (Fig. 12b). In the pre-wear period of 0–1 h stage, the volume fraction of RA decreases rapidly, while the impact wear resistance increases rapidly at this stage (Fig. 8b). The transformation of RA was contributed to the improvement of wear resistance. In addition, the full width at half-maximum (FWHM) of the diffraction peak also increased during impact wear progress. To further clarify the changes that occur in the FB specimens during impact wear progress, the increases in half-height widths were calculated by the classical Williamson-Hall in ΔK -K diagram as shown in Fig. 12c. Moreover, the dislocation density is reflected by FWHM. The increase in dislocation density caused by micro-strain is shown in Fig. 12d. The dislocation density rises rapidly initially and then tends to be stable Table 3.

3.5 Fatigue Test

A fatigue test was designed to clarify the different wear resistance of FB and H400 specimens caused by fatigue crack propagation in impact wear. The whole process of the FB and H400 specimens from steady state to instability can be characterized by the micro-force fatigue tester, similar to the weight loss caused by the initiation and propagation of fatigue cracks on the subsurface during impact wear. The loading force curve of H400 (Fig. 13a) shows the whole fatigue process of the material, from steady state to fracture. Stage I is the stable stage. When the cycle number reached 200,000 times, H400 entered the crack instability stage (stage II). The crack propagation reduced the stress area and caused the stress to decrease rapidly. The fatigue process of FB specimens was accompanied by continuous hardening and failure.

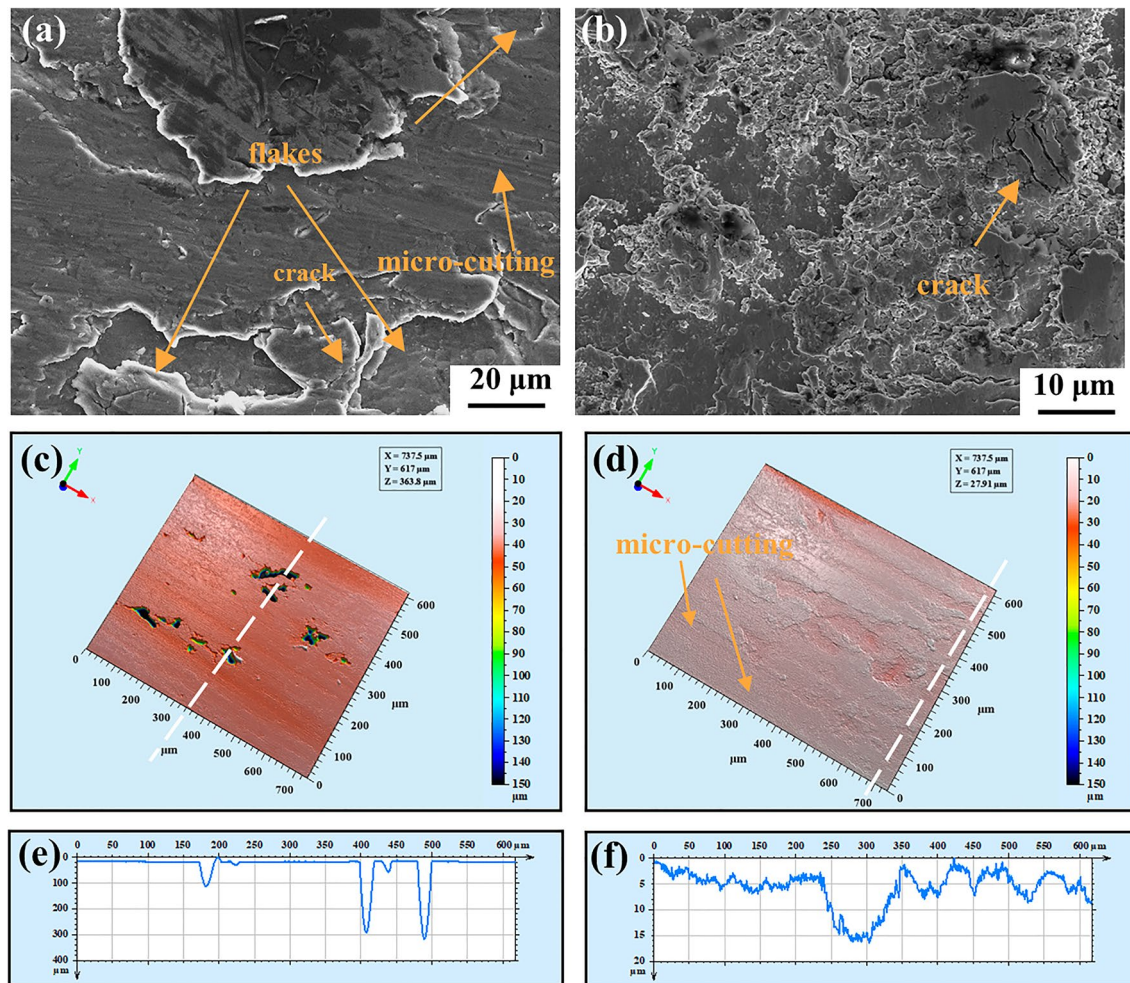


Fig. 10 SEM micrographs of wear surface of **a** H400 and **b** FB specimens; three-dimensional wear surface of **c** H400 and **d** FB; depth of cross-section statistics for **e** H400 and **f** FB specimens

4 Discussion

4.1 Wear Resistance of FB and H400 Specimens

H400 and FB specimens exhibited different wear resistance under three-body abrasive wear and impact wear conditions. The hardness of H400 specimen was uniform, and there was no area where the hardness was too low (Fig. 6). H400 specimen exhibited well resistance to abrasive embedding and broken abrasives. Broken abrasives were not embedded in the deep positions of the matrix. Therefore, the cutting action of the abrasive could only affect the shallow areas of the wear surface of the H400 specimen. The hardness of RA in the FB specimen was low and could not resist the embedding of high-hardness abrasives. Moreover, when abrasives were embedded in the matrix through RA, stress concentration was likely to occur near the abrasives, leading to crack initiation and accelerating the abrasives' cutting action. In addition, the

work-hardening behavior during wear progress increased the surface hardness (Fig. 8c), which improved the ability of H400 and FB specimens to resist cutting by abrasives, thus enhancing wear resistance. However, RA had a negative role on the wear resistance in the early wear stage, making the wear resistance of FB specimens consistently lower than that of H400. Uniform hardness contributes to higher wear resistance under three-body abrasive wear.

The FB specimen exhibited better wear resistance under impact wear condition. The increased wear resistance due to work-hardening behavior was also found during impact wear process (Fig. 11a and c). However, the wear resistance of FB increased rapidly at the early stage of wear (Fig. 9b), which may be related to the TRIP effect of RA. The transformation of RA under impact wear condition will be discussed in detail in Sect. 4.2. In addition, the mass loss caused by fatigue spalling under impact wear process deserves attention. The FB and H400 specimens exhibited different resistance to fatigue cracking under impact loading, as evidenced

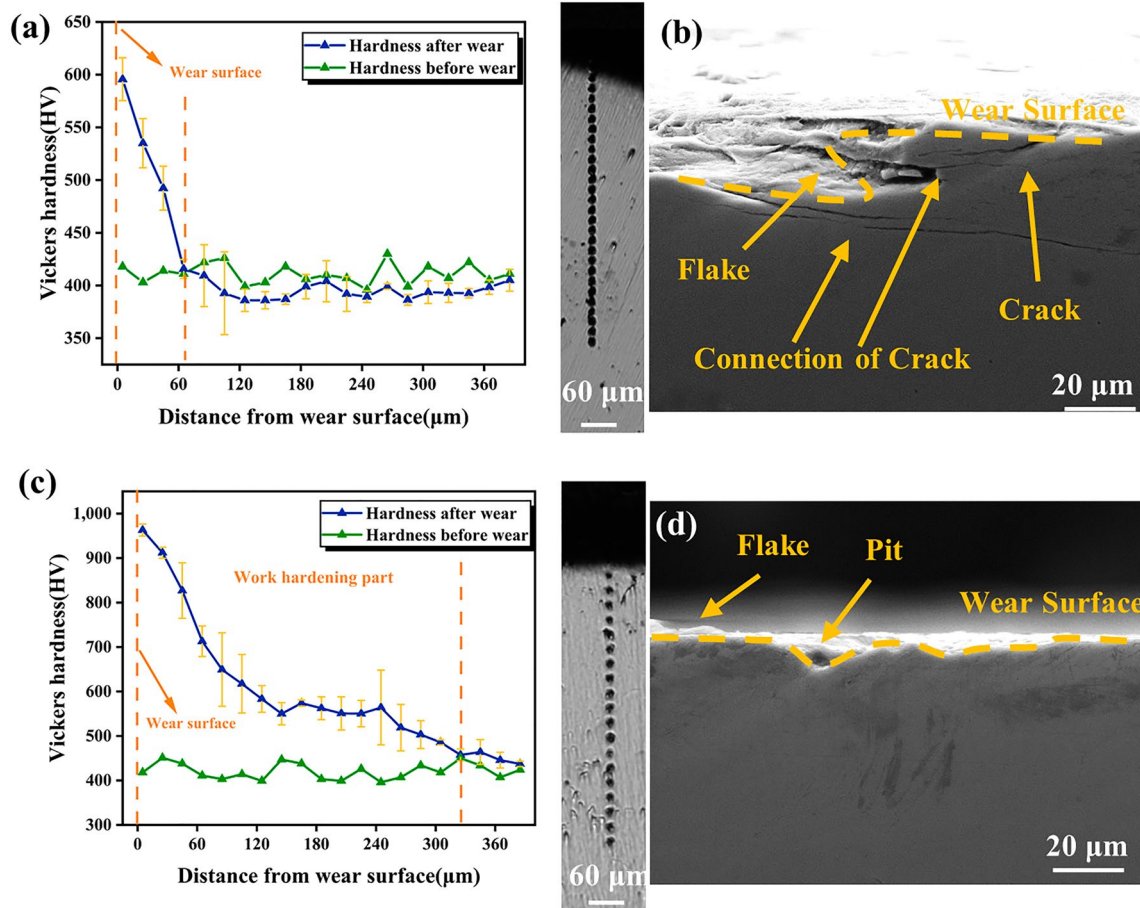


Fig. 11 The hardness of distance from wear surface in impact wear of **a** H400 and **c** FB specimens; SEM of Wear surface cross-sectional directional in impact wear of **b** H400 and **d** FB specimens

by the subsurface observed in Fig. 11b and d. Further discussions on fatigue cracking are described in Sect. 4.3.

In general, the microstructure between FB and H400 under different wear conditions is the main reason for the difference in wear behavior. The different effects of RA, cutting by abrasives or the TRIP effect, lead to the change of wear resistance of FB specimens under different wear conditions. The discussion of wear resistance should be under a specific wear condition.

4.2 The Evolution of the Microstructure and Dislocation Density During Impact Wear Process

Diffraction peaks broadening is associated with wear process, which can also increase strain-generated dislocation density [36, 37]. The increased dislocation density in FB specimens could be attributed to the existence of RA. RA with low dislocation density could accommodate more dislocations caused by deformation under impact wear process [38]. In addition, the deformation-induced martensite

transformation of RA consumed the internal dislocations. And the transformation of RA is in the order of blocky to film, under the action of strain, this gradual and sufficient TRIP effect produces a high strain-hardening rate, improving both strength and ductility of the forged steels [39]. In conclusion, The RA in FB specimen could accommodate more deformation at the early stage of impact wear progress. The accumulated deformation led to a corresponding increase in dislocation density. RA was completely transformed in the late stage of impact wear progress, and the dislocation density reached dynamic equilibrium. During this process, the increase of FWHM and dislocation density represents the ability of the material to accommodate defects.

4.3 Fatigue Crack Initiation and Propagation Behavior

The microstructure of H400 and FB specimens caused the difference in the cycle number to failure. Firstly, the bainitic structure exhibited better ductility and toughness, and relatively better deformability than martensite

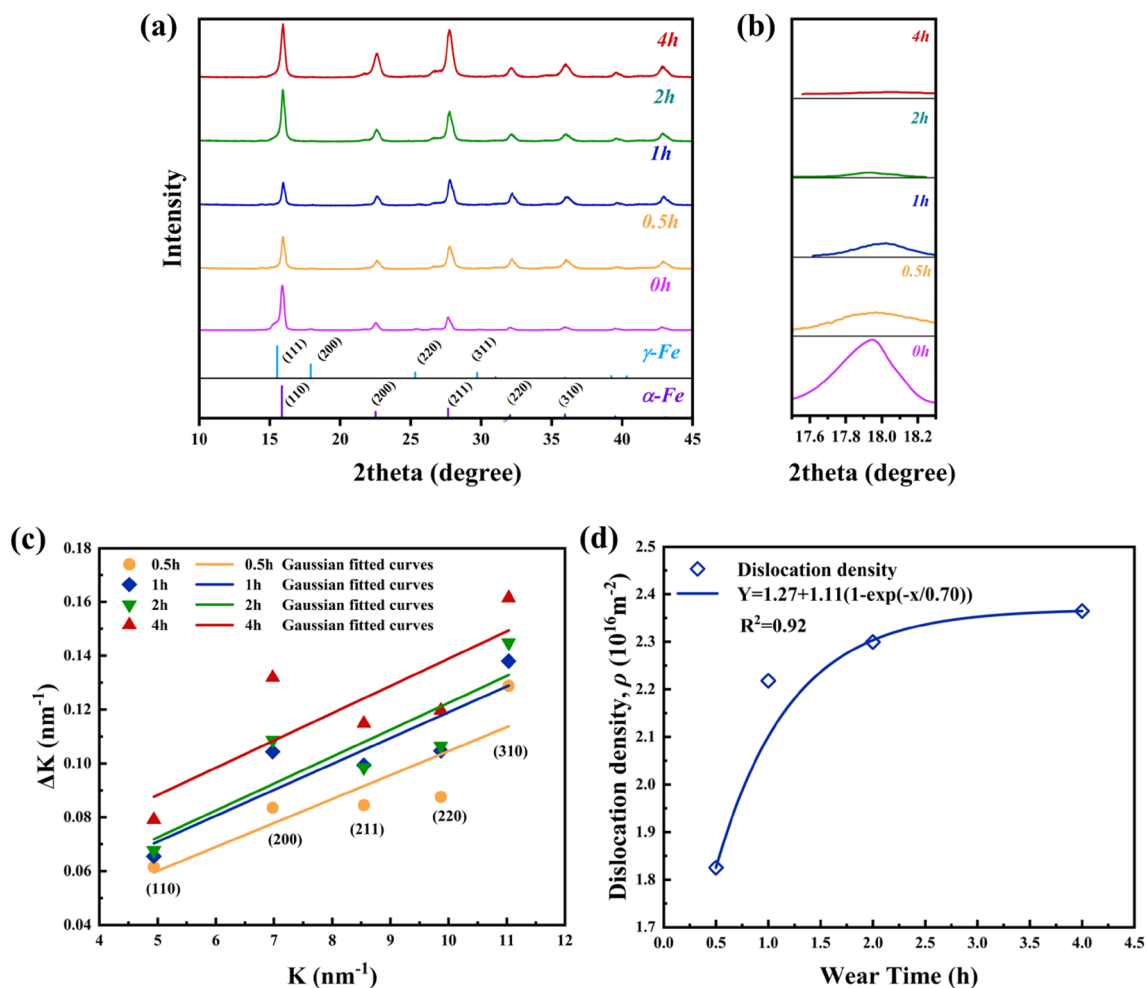


Fig. 12 XRD pattern and the partial enlarged detail of RA in FB specimen at (a) and (b); **c** the classical Williamson-Hall in ΔK - K diagram ($\Delta K = \beta \frac{\cos\theta}{\lambda}$, $K = \frac{2\sin\theta}{\lambda}$); **d** dislocation density during impact wear progress

[40–42]. Secondly, compared with H400 specimen, the FB specimen contained relatively few crack nucleation sites. H400 specimen displayed a lath martensite structure with relatively high dislocation density, which could easily cause micro-strain concentration and fatigue cracks. The FB specimen was composed of martensitic, bainite and RA with relatively low dislocation density. Interestingly, dislocation recovery occurred in bainitic laths during fatigue [43]. Crack initiation is inevitable in the

deformation process, and the crack propagation rate is also an important factor leading to fatigue failure. RA in the FB specimen could effectively reduce the crack propagation energy and thus slow down the growth rate of the fatigue crack. On the one hand, the expanding fatigue crack will change direction when encountering B-RA, thus consuming energy [44–46]. On the other hand, when the fatigue crack tip propagates to RA in the FB specimen, RA will absorb the crack propagation energy and transform to martensite [44, 47]. The deformation-induced martensitic transformation was also accompanied by volume expansion [48, 49], which could close microcracks [49, 50]. In addition, the bainite structure also exhibited the effect of inhibiting the propagation of microcracks [51]. The above factors caused the difference in resistance to fatigue cracks initiation and propagation between H400 and FB specimens. The dislocation propagation provided conditions for crack nucleation. Under impact wear with fatigue spalling as the primary wear mechanism, the FB specimen obtained

Table 3 Gaussian fitted curve for K-K after wear

Time (h)	Gaussian fitted curve of peak spreading after wear
0.5	$F(x) = 0.0089x + 0.00286$
1	$F(x) = 0.00961x + 0.00273$
2	$F(x) = 0.00999x + 0.00326$
4	$F(x) = 0.01013x + 0.00414$

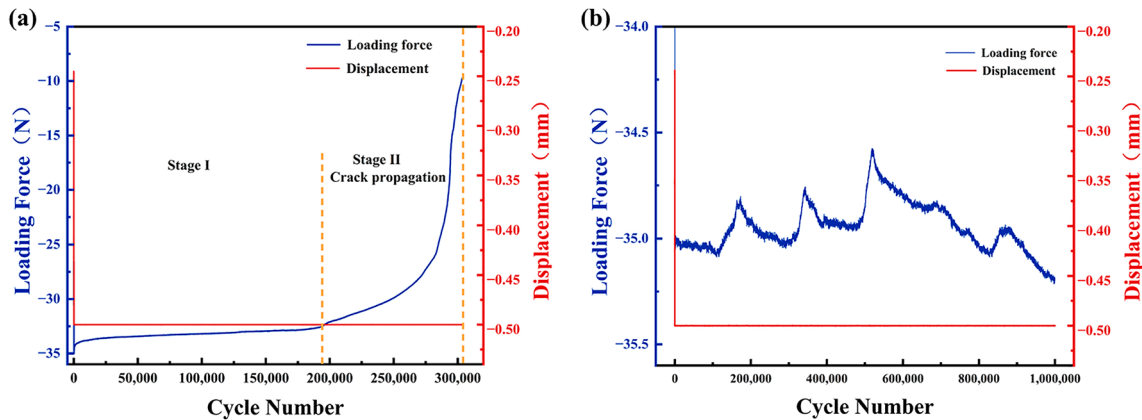


Fig. 13 Fatigue process loading force and displacement—cycle number curve of **a** H400 and **b** FB

high wear resistance due to its good resistance to crack initiation and propagation.

5 Conclusions

In this study, RA enhanced the impact wear resistance of FB, whereas it was the complete opposite under three-body abrasive wear. Comparing FB to H400, in terms of the differences in microstructures, mechanical properties, and wear behaviors, the following conclusions were drawn:

1. FB, a multiphase wear-resistant steel composed of bainite, martensite, and RA, exhibited limited hardness as low as 362 HV and better UTS and TE as high as 1399 MPa and 13.57%, respectively. In addition, the TRIP effect of RA improved its strength and plasticity.
2. The cumulative weight loss of H400 after the three-body abrasive wear became lower by 14.66%. The martensite structure with high and uniform hardness of H400 specimen contributed to good wear resistance under three-body abrasive wear condition. The key to maintaining a high wear resistance under three-body abrasive wear is to resist abrasive embedment and cutting.
3. The main takeaway is that FB had better wear resistance during the impact wear process owing to the inhibition of fatigue crack propagation. The deformation-induced martensite transformation rapidly increased the hardness of the wear surface, which could accommodate more dislocation. The FB specimen had better fatigue performance, because the transformation of RA alleviated the stress concentration and the TRIP effect enhanced plasticity to delay the fatigue fracture of the FB. Wear-resistant steel, without sufficient plasticity and fatigue properties, is unsuitable for impact wear conditions.

Author Contributions PC designed the experiment and wrote the main manuscript text. QH participated in the X-ray diffraction experiment. All authors reviewed the manuscript. QS provided the financial support.

Funding This work was supported by National Natural Science Foundation of China [Grant No. 52071167], the Science Foundation for Outstanding Youth of Yunnan Province [Grant No. 202201AW070004], the Science Foundation of the Yunnan Provincial Science and Technology Department [Grant No. 202101AT070074], and the Science and Technology Major Project of Yunnan Province [Grant No. 202202AG050011] for financial support.

Declarations

Conflict of interest The authors declare that they have no known competing financial interests or personal relationships that could have appeared to influence the work reported in this paper.

References

1. Qiu, B., Xing, S., Dong, Q., Liu, H.: Comparison of properties and impact abrasive wear performance of ZrO_2 - Al_2O_3 /Fe composite prepared by pressure casting and infiltration casting process. *Tribol. Int.* **142**, 105979 (2020). <https://doi.org/10.1016/j.triboint.2019.105979>
2. Inthidech, S., Opapaiboon, J., Yamamoto, K., Matsubara, Y.: Three-body-type Abrasive wear behavior of multi-alloyed white cast iron with different carbon contents used for hot work rolls. *ISIJ Int.* **61**, 2832–2843 (2021). <https://doi.org/10.2355/isijinternational.ISIJINT-2021-035>
3. Roscioli, G., Taheri-Mousavi, S.M., Tasan, C.C.: How hair deforms steel. *Science* **369**, 689–694 (2020). <https://doi.org/10.1126/science.aba9490>
4. Jafari, A., Dehghani, K., Bahaaddini, K., Hataie, R.A.: Experimental comparison of abrasive and erosive wear characteristics of four wear-resistant steels. *Wear* **416**, 14–26 (2018)
5. Kostyryzhev, A.G., Killmore, C.R., Yu, D., Pereloma, E.V.: Martensitic wear resistant steels alloyed with titanium. *Wear* **446**, 203203 (2020). <https://doi.org/10.1016/j.wear.2020.203203>
6. Tripathi, K., Gyawali, G., Lee, S.W.: Graphene coating via chemical vapor deposition for improving friction and wear of gray cast

- iron at interfaces. *ACS Appl. Mater. Interfaces* **9**, 32336–32351 (2017). <https://doi.org/10.1021/acsami.7b07922>
7. Li, D., Wang, Y., Wang, C., Li, S.: Research on the Wear behavior of the fixed cone liner of a cone crusher based on the discrete element method. *ACS Omega* **5**, 11186–11195 (2020). <https://doi.org/10.1021/acsomega.0c01272>
 8. Liu, W., Jiang, Y., Liu, H., Zhao, A.: A study of wear resistance of carbon-free bainite and martensite in medium carbon steel. *Ironmak. Steelmak.* **47**, 1056–1062 (2020). <https://doi.org/10.1080/03019233.2019.1666526>
 9. Efremenko, V.G., Hesse, O., Friedrich, T., Kunert, M., Brykov, M.N., Shimizu, K., Zurnadzhly, V.I., Šuchmann, P.: Two-body abrasion resistance of high-carbon high-silicon steel: metastable austenite vs nanostructured bainite. *Wear* **418–419**, 24–35 (2019). <https://doi.org/10.1016/j.wear.2018.11.003>
 10. Shah, M., Das Bakshi, S.: Three-body abrasive wear of carbide-free bainite, martensite and bainite-martensite structure of similar hardness. *Wear* **402**, 207–215 (2018). <https://doi.org/10.1016/j.wear.2018.02.020>
 11. Wei, Z., Wang, W., Liu, M., Tian, J., Xu, G.: Comparison of wear performance of bainitic and martensitic structure with similar fracture toughness and hardness at different wear conditions. *Wear* **512**, 204512 (2023). <https://doi.org/10.1016/j.wear.2022.204512>
 12. Zhang, H., Sun, M., Liu, Y., Ma, D., Xu, B., Huang, M., Li, D., Li, Y.: Ultrafine-grained dual-phase maraging steel with high strength and excellent cryogenic toughness. *Acta Mater.* **211**, 116878 (2021). <https://doi.org/10.1016/j.actamat.2021.116878>
 13. Zhou, Q., Qian, L., Meng, J., Zhao, L.: The fatigue properties, microstructural evolution and crack behaviors of low-carbon carbide-free bainitic steel during low-cycle fatigue. *Mater. Sci. Eng.* **820**, 141571 (2021). <https://doi.org/10.1016/j.msea.2021.141571>
 14. Wang, M., Huang, M.X.: Abnormal TRIP effect on the work hardening behavior of a quenching and partitioning steel at high strain rate. *Acta Mater.* **188**, 551–559 (2020). <https://doi.org/10.1016/j.actamat.2020.02.035>
 15. Seo, E.J., Cho, L., Estrin, Y., De Cooman, B.C.: Microstructure-mechanical properties relationships for quenching and partitioning (Q&P) processed steel. *Acta Mater.* **113**, 124–139 (2016). <https://doi.org/10.1016/j.actamat.2016.04.048>
 16. Liu, L., He, B.B., Cheng, G.J., Yen, H.W., Huang, M.X.: Optimum properties of quenching and partitioning steels achieved by balancing fraction and stability of retained austenite. *Scr. Mater.* **150**, 1–6 (2018). <https://doi.org/10.1016/j.scriptamat.2018.02.035>
 17. Liu, B., Li, W., Lu, X., Jia, X., Jin, X.: The effect of retained austenite stability on impact-abrasion wear resistance in carbide-free bainitic steels. *Wear* **428–429**, 127–136 (2019). <https://doi.org/10.1016/j.wear.2019.02.032>
 18. Ge, S., Wang, Q., Wang, J.: The impact wear-resistance enhancement mechanism of medium manganese steel and its applications in mining machines. *Wear* **376–377**, 1097–1104 (2017). <https://doi.org/10.1016/j.wear.2017.01.015>
 19. Deng, X., Huang, L., Wang, Q., Fu, T., Wang, Z.: Three-body abrasion wear resistance of TiC-reinforced low-alloy abrasion-resistant martensitic steel under dry and wet sand conditions. *Wear* **452**, 203310 (2020). <https://doi.org/10.1016/j.wear.2020.203310>
 20. Huang, L., Deng, X., Li, C., Jia, Y., Wang, Q., Wang, Z.: Effect of TiC particles on three-body abrasive wear behaviour of low alloy abrasion-resistant steel. *Wear* **434**, 202971 (2019). <https://doi.org/10.1016/j.wear.2019.202971>
 21. Akama, D., Tsuchiyama, T., Takaki, S.: Change in dislocation characteristics with cold working in ultralow-carbon martensitic steel. *ISIJ Int.* **56**, 1675–1680 (2016). <https://doi.org/10.2355/isijinternational.ISIJINT-2016-140>
 22. Tan, X., Xu, Y., Yang, X., Wu, D.: Microstructure-properties relationship in a one-step quenched and partitioned steel. *Mater. Sci. Eng.* **589**, 101–111 (2014). <https://doi.org/10.1016/j.msea.2013.09.063>
 23. Shan, Q., Ge, R., Li, Z., Zhou, Z., Jiang, Y., Lee, Y.-S., Wu, H.: Wear properties of high-manganese steel strengthened with nano-sized V₂C precipitates. *Wear* **482**, 203922 (2021). <https://doi.org/10.1016/j.wear.2021.203922>
 24. Moghaddam, P.V., Rinaudo, M., Hardell, J., Vuorinen, E., Prakash, B.: Influence of fracture toughness on two-body abrasive wear of nanostructured carbide-free bainitic steels. *Wear* **460**, 203484 (2020). <https://doi.org/10.1016/j.wear.2020.203484>
 25. Grajcar, A., Skowronek, A., Radwański, K.: Mechanical behavior and stability of dispersed retained austenite in thermomechanically rolled and isothermally-treated TRIP-aided multiphase steel. *Mater. Sci. Eng.* **830**, 142300 (2022). <https://doi.org/10.1016/j.msea.2021.142300>
 26. Wang, K., Gui, X., Bai, B., Gao, G.: Effect of tempering on the stability of retained austenite in carbide-free bainitic steel. *Mater. Sci. Eng.* **850**, 143525 (2022). <https://doi.org/10.1016/j.msea.2022.143525>
 27. Wang, T.S., Yang, J., Shang, C.J., Li, X.Y., Zhang, B., Zhang, F.C.: Microstructures and impact toughness of low-alloy high-carbon steel austempered at low temperature. *Scr. Mater.* **61**, 434–437 (2009). <https://doi.org/10.1016/j.scriptamat.2009.04.038>
 28. Zhao, J., Zhang, F.: In-situ observation of tensile deformation and retained austenite transformation behaviors in carbide-free bainitic steel. *Mater. Sci. Eng.* **771**, 138637 (2020). <https://doi.org/10.1016/j.msea.2019.138637>
 29. Hu, B., He, B., Cheng, G., Yen, H., Huang, M., Luo, H.: Super-high-strength and formable medium Mn steel manufactured by warm rolling process. *Acta Mater.* **174**, 131–141 (2019). <https://doi.org/10.1016/j.actamat.2019.05.043>
 30. Wang, C.Y., Shi, J., Cao, W.Q., Dong, H.: Characterization of microstructure obtained by quenching and partitioning process in low alloy martensitic steel. *Mater. Sci. Eng.* **527**, 3442–3449 (2010). <https://doi.org/10.1016/j.msea.2010.02.020>
 31. Zhao, L., Wang, Q., Shi, G., Yang, X., Qiao, M., Wu, J., Zhang, F.: In-depth understanding of the relationship between dislocation substructure and tensile properties in a low-carbon microalloyed steel. *Mater. Sci. Eng.* **854**, 143681 (2022). <https://doi.org/10.1016/j.msea.2022.143681>
 32. Dong, H.Y., Wu, K.M., Wang, X.L., Hou, T.P., Yan, R.: A comparative study on the three-body abrasive wear performance of Q&P processing and low-temperature bainitic transformation for a medium-carbon dual-phase steel. *Wear* **402**, 21–29 (2018). <https://doi.org/10.1016/j.wear.2018.01.009>
 33. Luo, Z.C., Ning, J.P., Wang, J., Zheng, K.H.: Microstructure and wear properties of TiC-strengthened high-manganese steel matrix composites fabricated by hypereutectic solidification. *Wear* **432**, 202970 (2019). <https://doi.org/10.1016/j.wear.2019.202970>
 34. Dalai, R., Das, S., Das, K.: Effect of thermo-mechanical processing on the low impact abrasion and low stress sliding wear resistance of austenitic high manganese steels. *Wear* **420**, 176–183 (2019). <https://doi.org/10.1016/j.wear.2018.10.013>
 35. Peng, S.-G., Song, R.-B., Sun, T., Yang, F.-Q., Deng, P., Wu, C.-J.: Surface failure behavior of 70Mn martensite steel under abrasive impact wear. *Wear* **362–363**, 129–134 (2016). <https://doi.org/10.1016/j.wear.2016.05.019>
 36. Das Bakshi, S., Leiro, A., Prakash, B., Bhadeshia, H.K.D.H.: Dry rolling/sliding wear of nanostructured bainite. *Wear* **316**, 70–78 (2014). <https://doi.org/10.1016/j.wear.2014.04.020>
 37. Dong, G., Wang, J., Wang, L., Wang, C., Hu, J., Xu, W.: Transitions in the thermal stability of pre-strained austenite—competing effects between defect density and slip band spacing. *Scr. Mater.* **223**, 115077 (2023). <https://doi.org/10.1016/j.scriptamat.2022.115077>

38. Long, X., Zhang, R., Zhang, F., Du, G., Zhao, X.: Study on quasi-in-situ tensile deformation behavior in medium-carbon carbide-free bainitic steel. *Mater. Sci. Eng.* **760**, 158–164 (2019). <https://doi.org/10.1016/j.msea.2019.05.112>
39. Li, Y., Yuan, G., Li, L., Kang, J., Yan, F., Du, P., Raabe, D., Wang, G.: Ductile 2-GPa steels with hierarchical substructure. *Science* **379**, 168–173 (2023). <https://doi.org/10.1126/science.add7857>
40. Abbaszadeh, K., Saghafian, H., Kheirandish, S.: Effect of bainite morphology on mechanical properties of the mixed bainite-martensite microstructure in D6AC steel. *J. Mater. Sci. Technol.* **28**, 336–342 (2012). [https://doi.org/10.1016/S1005-0302\(12\)60065-6](https://doi.org/10.1016/S1005-0302(12)60065-6)
41. Long, X.Y., Kang, J., Lv, B., Zhang, F.C.: Carbide-free bainite in medium carbon steel. *Mater. Des.* **64**, 237–245 (2014). <https://doi.org/10.1016/j.matdes.2014.07.055>
42. Hasan, S.M., Mandal, A., Singh, S.B., Chakrabarti, D.: Work hardening behaviour and damage mechanisms in carbide-free bainitic steel during uni-axial tensile deformation. *Mater. Sci. Eng.* **751**, 142–153 (2019). <https://doi.org/10.1016/j.msea.2019.02.062>
43. Mi, B., Yang, Z., Chen, H., Zhang, C.: Quasi in-situ observations of microstructure evolution during low cycle fatigue in carbide-free bainitic steel. *Int. J. Fatigue* **168**, 107464 (2023). <https://doi.org/10.1016/j.ijfatigue.2022.107464>
44. Kumar, A., Singh, A.: Microstructural effects on the sub-critical fatigue crack growth in nano-bainite. *Mater. Sci. Eng.* **743**, 464–471 (2019). <https://doi.org/10.1016/j.msea.2018.11.114>
45. Zhou, S.-B., Hu, C.-Y., Hu, F., Cheng, L., Isayev, O., Yershov, S., Xiang, H.-J., Wu, K.-M.: Insight into the impact of microstructure on crack initiation/propagation behavior in carbide-free bainitic steel during tensile deformation. *Mater. Sci. Eng.* **846**, 143175 (2022). <https://doi.org/10.1016/j.msea.2022.143175>
46. Królicka, A., Lesiuk, G., Radwański, K., Kuziak, R., Janik, A., Mech, R., Zygmunt, T.: Comparison of fatigue crack growth rate: pearlitic rail versus bainitic rail. *Int. J. Fatigue* **149**, 106280 (2021). <https://doi.org/10.1016/j.ijfatigue.2021.106280>
47. Yang, J., Wang, T.S., Zhang, B., Zhang, F.C.: High-cycle bending fatigue behaviour of nanostructured bainitic steel. *Scr. Mater.* **66**, 363–366 (2012). <https://doi.org/10.1016/j.scriptamat.2011.11.033>
48. Koyama, M., Zhang, Z., Wang, M., Ponge, D., Raabe, D., Tsuzaki, K., Noguchi, H., Tasan, C.C.: Bone-like crack resistance in hierarchical metastable nanolaminate steels. *Science* **355**, 1055–1057 (2017). <https://doi.org/10.1126/science.aal2766>
49. Gao, G., Liu, R., Wang, K., Gui, X., Misra, R.D.K., Bai, B.: Role of retained austenite with different morphologies on sub-surface fatigue crack initiation in advanced bainitic steels. *Scr. Mater.* **184**, 12–18 (2020). <https://doi.org/10.1016/j.scriptamat.2020.03.036>
50. Wang, X., Liu, C., Sun, B., Ponge, D., Jiang, C., Raabe, D.: The dual role of martensitic transformation in fatigue crack growth. *Proc. Natl. Acad. Sci. U.S.A.* **119**, e2110139119 (2022). <https://doi.org/10.1073/pnas.2110139119>
51. Long, X., Zhao, G., Zhang, F., Xu, S., Yang, Z., Du, G., Branco, R.: Evolution of tensile properties with transformation temperature in medium-carbon carbide-free bainitic steel. *Mater. Sci. Eng.* **775**, 138964 (2020). <https://doi.org/10.1016/j.msea.2020.138964>

Publisher's Note Springer Nature remains neutral with regard to jurisdictional claims in published maps and institutional affiliations.

Springer Nature or its licensor (e.g. a society or other partner) holds exclusive rights to this article under a publishing agreement with the author(s) or other rightsholder(s); author self-archiving of the accepted manuscript version of this article is solely governed by the terms of such publishing agreement and applicable law.